# Thermally activated plastic flow in the presence of multiple obstacle types

You may also be interested in:

# Thermally activated plastic flow in the presence of multiple obstacle types

## Y Dong[1] and W A Curtin[2]

[1] School of Engineering, Brown University, Providence, RI, 02912, USA
[2] Institute of Mechanical Engineering, EPFL, 1015 Lausanne, Switzerland

E-mail: william.curtin@epfl.ch

## Abstract

The rate- and temperature-dependent plastic flow in a material containing two types of thermally activatable obstacles to dislocation motion is studied both numerically and theoretically in a regime of relative obstacle densities for which the zero-temperature stress is additive. The numerical methods consider the low-density 'forest' obstacles first as point obstacles and then as extended obstacles having a finite interaction length with the dislocation, while the high-density 'solute' obstacles are treated as point obstacles. Results show that the finite-temperature flow stresses due to different obstacle strengthening mechanisms are additive, as proposed by Kocks *et al*, only when all strengthening obstacles can be approximated as point-like obstacles. When the activation distance of the low-density extended obstacles exceeds the spacing between the high-density obstacles, the finite-temperature flow stress is non-additive and the effective activation energy differs from that of the Kocks *et al* model. An analytical model for the activation energy versus flow stress is proposed, based on analysis of the simulation results, to account for the effect of the finite interaction length. In this model, for high forest activation energies, the point-pinning solute obstacles provide a temperature-dependent backstress $\sigma_b$ on dislocation and the overall activation energy is otherwise controlled by the forest activation energy. The model predictions agree well with numerical results for a wide range of obstacle properties, clearly showing the effect due to the finite interaction between dislocation and the obstacles. The implications of our results on the activation volume are discussed with respect to experimental results on solute-strengthened fcc alloys.

(Some figures may appear in colour only in the online journal)

## 1. Introduction

The flow stress of polycrystalline metallic materials is determined by the resistance encountered by a dislocation as it glides through a field of obstacles such as solute atoms, forest dislocations or precipitates. The detailed mechanics of the strengthening by obstacles is crucial for the design of metallic alloys, and has been widely studied at various scales [1–7]. In most engineering alloys, the flow stress is controlled by several different obstacle types such as forest dislocations plus solutes and/or precipitates operating simultaneously, and therefore a clear understanding of how different strengthening mechanisms operate together to generate a macroscopically measured flow stress is required. 'Flow stress' is, however, also dependent on both temperature and strain rate, reflecting the fact that dislocations can overcome obstacles through thermally activated processes [8, 9]. In spite of considerable experimental and theoretical efforts over the course of many decades, a full picture of thermally activated plastic flow in the presence of multiple obstacle types does not yet exist.

At zero temperature, the flow stress in the presence of multiple types of point obstacles has been reasonably well studied. Given zero-temperature flow stresses $\hat{\sigma}_1$ and $\hat{\sigma}_2$ for two different mechanisms acting separately, a general superposition rule $\hat{\sigma}^\alpha = \hat{\sigma}_1^\alpha + \hat{\sigma}_2^\alpha$ [8, 10, 11] for the total flow stress $\hat{\sigma}$ has been found to explain simulations [12–15] and used to interpret experiments [16–18], where the exponent $1 \leqslant \alpha \leqslant 2$ depends on details of obstacle densities and relative strengths. Specifically, in the limit where the obstacle densities vary considerably, $\rho_1 \gg \rho_2$, we have recently shown that $\alpha = 1$ [19], i.e. linear superposition, applies independent of the value $\hat{\sigma}_1$ and $\hat{\sigma}_2$. This limit is thought to apply to solute-strengthened materials where both forest hardening ($\hat{\sigma}_1, \rho_1$) and solute hardening ($\hat{\sigma}_1, \rho_2$) operate. Linear superposition also emerges immediately if the solute strengthening is modeled as a continuous friction stress. However, even the friction limit must be treated with care, since Monnet and Devincre have used discrete dislocation simulations to show that the linear additivity is lost as the friction stress increases, due to the changes in forest-junction length and formed junction density [20], leading to $\alpha > 1$.

Via thermal activation, dislocations can surpass obstacles so that the flow stress $\sigma$ is a function of strain rate $\dot{\varepsilon}$ and temperature $T$. It is well established [5, 8, 9] that the macroscopic strain rate can be related to the change in the Gibbs free energy $\Delta G$ [8] via an Arrhenius-type rate equation. $\Delta G$ is essentially the energy barrier required for thermal activation of dislocation across an obstacle. In this general frame, the thermally activated motion of the dislocation and associated macroscopic strain rate can be characterized by some function involving $\Delta G$, $\sigma$ and $T$. The strain rate sensitivity (SRS), $m = \partial \ln \dot{\varepsilon} / \partial \ln \sigma$, and the apparent activation area, $\Delta a = -\frac{1}{b} \frac{\partial \Delta G}{\partial \sigma}$, can then be compared with experiments. The thermally activated behavior of dislocations through a field consisting of a single type of obstacle has been studied numerically for years [21–23], where it is shown that factors such as the obstacle strength, density and spatial distribution have strong influences on the flow behavior.

Owing to the complexity of possible mechanisms, the simultaneous operation of and interactions between different strengthening mechanisms operating together at finite temperature remains far less clear. The first question regarding the superposition of flow stress at finite temperature is how the individual strengths should be measured. As pointed out by Kocks *et al* [8, 24] and Diak [25], the flow stresses for different mechanisms must be defined at the same $\dot{\varepsilon}$ and $T$. Building on this foundation, a natural and simple idea is to extend the linear additivity at zero temperature to finite temperature [8], i.e. $\sigma(\dot{\varepsilon}, T) = \sigma_1(\dot{\varepsilon}, T) + \sigma_2(\dot{\varepsilon}, T)$. As a result, linear additivity of the inverse activation area emerges. However, linear additivity cannot predict the reduced slope of the Haasen plot found in experiments of solute-strengthened alloys [25–29]. The general superposition rule can be extended also,

i.e. $\sigma^\alpha(\dot{\varepsilon}, T) = \sigma_1^\alpha(\dot{\varepsilon}, T) + \sigma_2^\alpha(\dot{\varepsilon}, T)$, but without fundamental justification [25, 30, 31]. Schoeck [32] theoretically studied the thermally activated motion of a dislocation line in a field containing a low density of obstacles with high activation energy and a high density of obstacles having low activation energy. He concluded that the linear additivity at finite temperature did not follow from linear additivity at $T = 0$. Aresenault and Cadman [33] simulated the thermal motion of a dislocation across a random array of point obstacles having different strengths and zero-stress activation energies at finite temperature. Their simulations gave an overall flow stress $\sigma(\dot{\varepsilon}, T)$ lying between $\sigma_1(\dot{\varepsilon}, T) + \sigma_2(\dot{\varepsilon}, T)$ and $(\sigma_1^2(\dot{\varepsilon}, T) + \sigma_2^2(\dot{\varepsilon}, T))^{1/2}$. In these studies, the relationship between the overall activation energy and the properties of individual obstacle type and the flow stress was not made clear. More recently, Xu and Picu [23] analyzed the SRS for a single type of point obstacle via simulations and developed a model to account for the variation of the SRS parameter $m$. The model was consistent with simulations at a low-stress level but deviated at high stresses. They argued that the different regimes for $m$ are associated with different mechanism of dislocation motion (smooth un-zipping mode at low stresses and jerky mode at high stresses). Subsequent simulations with multiple point obstacle type explored similar variation of $m$ with flow stress [34], showing that the SRS was very sensitive to the presence of obstacles with large strength and high activation energy. Insertion of even a small density of strong obstacles resulted in SRS behavior comparable to that of the strong obstacles operating alone. Picu *et al* thus suggested that linear additivity of flow stress at finite temperature would be valid only when the flow stresses due to individual strengthening were measured at the same SRS parameter [34, 35].

The above brief literature review shows that thermally activated flow in the presence of multiple strengthening mechanisms remains poorly understood and that the explicit form of the overall flow stress versus strain rate and temperature requires further development. Complicating the situation is that most numerical simulations are in a regime where the zero-temperature flow stresses themselves are not additive, making it particularly difficult to extract the interaction effects at finite temperature [33, 34]. Furthermore, simulations and theory have focused on point-pinning obstacle model, which neglects any influence of the interaction length between the dislocation and obstacles. However, the point-pinning assumption has to be treated with care since previous simulations have shown that, at zero temperature, the interaction width of the obstacles affects the way in which the dislocation samples the field of obstacles during glide, and thus affects the shear resistance of obstacles [36, 37]. In addition, for obstacles such as forest dislocation having high zero-stress activation energy and moderate strength, the physical obstacle interaction length scale (in the case of forest, the junction length) may not be negligible compared with the spacing of dispersed solute-type obstacles, calling into question the applicability of the point-pinning obstacle model for multiple obstacle types.

To address the above issues, we focus here on thermally activated flow in the case where the zero-temperature flow stress in known to be additive [19], and consider both point and extended-obstacle models for the forest obstacles. We compute, via simulation, the effective activation energy for dislocation escape across the field of combined obstacles types, and develop an analytical model for thermally activated flow stress based on numerical simulations. We show that the linear additivity of flow stress at finite temperature is valid only when all strengthening obstacles can be treated as point-like obstacles. Obstacles with finite interaction length and associated high activation energy result in a non-additive overall flow stress at finite temperature even while linear additivity holds at $T = 0$. Our simulations show that at low stresses, the high-density 'solute' obstacles provide a thermal backstress $\sigma_b$ acting on the dislocation, influencing the thermal activation over the extended 'forest' obstacles. An analytical model for the overall activation energy $\Delta G(\sigma, T)$ is then proposed based on the simulations and shown to agree well with simulations for a wide range of obstacle properties.
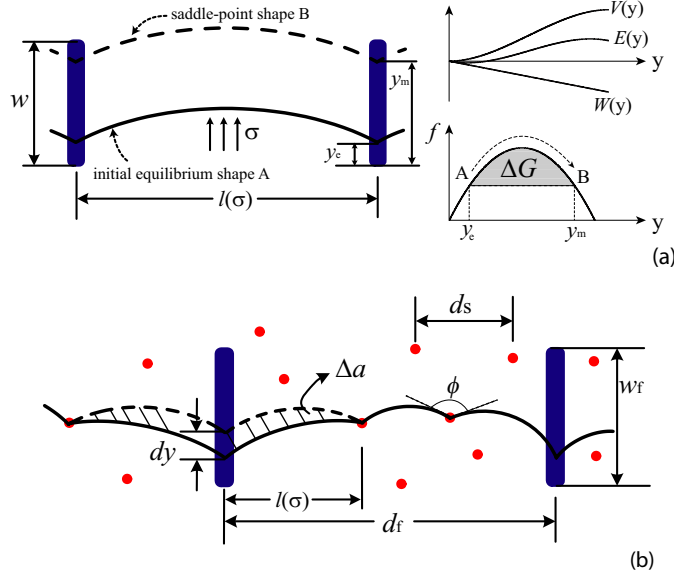
**Figure 1.** (*a*) Schematic of thermal activation for a dislocation bypassing obstacles with finite interaction length $w$; (*b*) schematic of the algorithm used in the extended obstacle model (see text). Blue bars: extended obstacles; red dots: point obstacles; black lines: mobile dislocation.

## 2. Simulation models for thermally activated flow

In this section, we describe the algorithms used to simulate the thermal motion of a dislocation line across a slip plane along which two different types of obstacles are present. The dislocation line is modeled as a flexible string with isotropic line tension $\Gamma = 0.5\mu b^2$, where $\mu$ is the shear modulus and $b$ is the magnitude of the Burgers vector. An initial dislocation of length $L$ will glide in a plane that contains a random array of point obstacles representing the weak solute 's' obstacles with density $1/d_s^2$, where $d_s$ is the average space between 's' obstacles. The overall simulation cell is a square of size $L \times L$ so that the number of 's' obstacles $N_s$ satisfies $L = d_s\sqrt{N_s}$. In all cases, we maintain $N_s \geqslant 40\,000$, a size sufficient to exclude finite-size effect in the simulations [38]. A single forest obstacle of type 'f' is positioned at the center of the glide plane. Periodic boundary conditions are applied on the lateral boundary of the square simulation cells so that the 'f' obstacles are effectively periodic with space $d_f = L$.

For thermal activation, we consider a typical case as illustrated in figure 1(*a*), where an obstacle interacts with the dislocation over a finite length $w$. The energy of the dislocation–obstacle interaction as a function of the distance $y$ measured along the direction of dislocation penetration into the obstacle can be expressed in terms of the zero-stress activation barrier $\Delta G^0$ and the interaction length $w$. The temperature dependence of the zero-stress activation energy $\Delta G^0$, arising from temperature-dependent material properties such as the elastic modulus and line tension, is neglected here so that our models are essentially isothermal models. Several energy profiles for dislocation–obstacle interaction have been proposed in former studies and summarized in [5, 9]. Here we introduce a third-order polynomial, which is simple but captures the essential physics [8, 39, 40]:

$$V(y) = \Delta G^0 \left( 3\left(\frac{y}{w}\right)^2 - 2\left(\frac{y}{w}\right)^3 \right) \tag{1}$$

4

and present an analysis along the lines of Kocks *et al* [8]. Accordingly, the resisting force on the dislocation can be expressed as

$$f(y) = \frac{\partial V}{\partial y} = \frac{6\Delta G^0}{w}\left(\left(\frac{y}{w}\right) - \left(\frac{y}{w}\right)^2\right) = 4f^c\left(\left(\frac{y}{w}\right) - \left(\frac{y}{w}\right)^2\right) \tag{2}$$

where $f^c = 3\Delta G^0/(2w)$ is the maximum resisting force of the obstacle. Under an applied stress $\sigma$, the dislocation will progress through the obstacle to an equilibrium distance $y_e$, with a force $f = \sigma b l(\sigma)$ exerted on the obstacle where $l(\sigma)$ is the characteristic spacing of obstacles on the dislocation line, as shown in figure 1(a). At the same force $f$, i.e. the same $\sigma$, there is also unstable equilibrium position $y_m$. The energy barrier that must be overcome to reach the unstable (saddle-point) configuration is

$$\Delta G = \Delta V - \Delta W, \tag{3}$$

where $\Delta V$ is the interaction energy difference from $y_e$ to $y_m$ and $\Delta W$ is the work done by $\sigma$ during the activation process, which are given by

$$\begin{aligned}
\Delta V &= V(y_m) - V(y_e) \\
\Delta W &= f(y_m - y_e) = \sigma b l(\sigma)(y_m - y_e)
\end{aligned} \tag{4}$$

$y_e$ and $y_m$ can be obtained by solving $dE/dy = 0$ where $E(y) = V(y) - W(y)$. Substituting solved $y_e$ and $y_m$ into equations (3) and (4) gives the activation energy

$$\Delta G = \Delta G^0\left(1 - \frac{f}{f^c}\right)^{3/2}. \tag{5}$$

The stress dependence of $\Delta G$ can be related to equation (5) for two cases. In the Friedel limit [3] for the randomly distributed weak obstacles, $l(\sigma) \sim \sigma^{-1/3}$ and $f \sim \sigma^{2/3}$ give

$$\Delta G = \Delta G^0\left(1 - \left(\frac{\sigma}{\hat{\sigma}}\right)^{2/3}\right)^{3/2}, \tag{6}$$

where $\hat{\sigma}$ is the flow stress at zero temperature. For a linear array of obstacles, $f \sim \sigma$ and thus $\Delta G$ follows

$$\Delta G = \Delta G^0\left(1 - \frac{\sigma}{\hat{\sigma}}\right)^{3/2}. \tag{7}$$

Based on the derivation above, each set of obstacles is now characterized by three parameters: the interaction length $w$; the zero-stress activation barrier $\Delta G^0$; and the average space $d$ which is related to the distance $l$. As shown in figure 1(b), at each pinning obstacle the two adjacent pinned dislocation segments define an angle $\phi$ and exert a force $f = \mu b^2 \cos(\phi/2)$ on the obstacle. The critical breaking angle $\phi^c$, at which point the force on the obstacle reaches the maximum resisting force, is thus related to the obstacle resistance $f^c$ and consequently gives $w = 3\Delta G/(4\Gamma\cos(\phi^c/2))$. Therefore, in simulations, $\phi^c$, $d$, and $\Delta G^0$ are used to define the different obstacles types, i.e. the set $\{d_s, \phi_s^c, \Delta G_s^0\}$ defines the properties of the 's' obstacles and the set $\{d_f, \phi_f^c, \Delta G_f^0\}$ for 'f' obstacles.

The algorithm developed by Nogaret and Rodney [38] for athermal simulations was modified to implement thermally activated dislocation motion. Briefly, a single dislocation is initially put at the bottom of the glide plane and its motion is described by a succession of incremental changes in the position of individual segment as the pining obstacles are overcome. For athermal simulations ($T = 0$), and to start thermally activated simulations, in any given dislocation configuration each segment will bow out until it (i) reaches the unstable half-circle configuration, where the bowing out radius of the segment equals one-half the distance between its pinning obstacles; (ii) meets a new obstacle; or (iii) breaks at a pinning point at which the

force has exceeded $f^c$. The stresses required for each of the three events are computed for all segments along the line, and the event and segment requiring the minimum stress among all events and all segments are selected. If this minimum stress is below the desired applied stress, then the dislocation is advanced to the next configuration based on the chosen event. If the minimum stress over all events is larger than the desired applied stress, then the dislocation is in a static equilibrium configuration and thermal activation is required for the dislocation to move further.

For thermally activated motion starting from a static equilibrium configuration, a kinetic Monte Carlo (kMC) procedure is introduced. Previous simulations [12, 13, 23, 34] normally ignored the details of the obstacle structure and directly implemented equation (5) to calculate the activation energy for a dislocation passing any pinning obstacle. We refer to this type of simulation as a 'Point-Pinning' simulation (PP simulation). In the PP simulation, at each static equilibrium configuration, the activation energy $\Delta G_i$ for the $i$th pinning obstacle is computed from the force $f_i$ via equation (5). The probability for overcoming the $i$th obstacle is computed as $p_i = \exp(-\frac{\Delta G_i}{k_B T})$, where $k_B$ is the Boltzmann's constant. The normalized cumulative probability for the $i$th obstacle $r_i$ is then calculated as $\sum_{j=1}^{i} p_j / \sum_{j=1}^{M} p_j$, where $M$ is the total number of obstacles that currently pin the dislocation line. A random number $R \in (0, 1)$ with uniform distribution is then chosen and the event $i$ that satisfies $r_{i-1} < R < r_i$ is chosen to advance the dislocation to a new configuration. The time required to accomplish this thermally activated step is $\Delta t = \left( \nu_0 \sum_{j=1}^{M} p_j \right)^{-1}$, where $\nu_0$ is the fundamental 'attempt' for escaping an obstacle [5]. The new dislocation configuration is then evaluated for any athermal event and, if any, is advanced to next static equilibrium configuration. The output from the PP simulation is the total time required for the dislocation to glide across the slip plane. Since the time spent in dislocation glide in between static equilibrium configuration is very short compared with the waiting time for each thermal activation event, the total time here is defined as the sum of the times consumed at each thermal activation event. The activation barrier for the overall process of escape through the field of obstacle is then derived from the total time $t_{tot}$ using the relationship

$$t_{tot}^{-1} = \nu_0 \exp\left(-\frac{\Delta G}{k_B T}\right) \tag{8}$$

leading to

$$\Delta G = k_B T \ln(\nu_0 t_{tot}). \tag{9}$$

Since $t_{tot}$ is measured in units of the $\nu_0^{-1}$, the resulting $\Delta G$ is independent of the value $\nu_0$.

The point-pinning limit ignores the influence of the interaction width $w$, that is, it assumes that $w \ll d$ and thus $w$ does not come into the consideration. This assumption might be applicable for distributed solute atoms or small precipitates [5, 36], but its applicability to forest strengthening is questionable. For forest dislocations, there is a moderate critical force but a large zero-stress activation energy [41], leading to a large interaction length $w_f$. In fact, simple models of forest-junction formation show that the junction length scales with the forest space itself [42, 43]. Most importantly for this work is the recognition that when both solute and forest mechanisms act together, treatment of the forests as point obstacle would also require $w_f \ll d_s$, which is unlikely to be valid. Therefore, the use of non-point-pinning model seems desirable, and perhaps essential, for the treatment of thermal activation in the presence of both solutes and forests.

We have thus developed an 'extended-obstacle' simulation (EO simulation) that uses the kMC-type algorithm schematically shown in figure 1(b) and is described as follows. At an applied stress $\sigma$, the dislocation is pinned by an extended 'f' obstacle with penetration

distance $y$ and also pinned by point-like 's' obstacles nearby. We then analyze a possible fluctuation of the dislocation position at the 'f' obstacle by a small distance $dy$. The energy change $\Delta E$ associated with this fluctuation is composed of the interaction energy change, $\Delta V = V(y+dy) - V(y)$, the work done by $\sigma$ as the dislocation glides between the surrounding pinning sites through some area $\Delta a$, $\Delta W = \sigma b \Delta a$, and the change in line energy due to the length change of the dislocation segments, $\Delta E_{\text{line}}$. The activation energy for this possible fluctuation is then $\Delta G = \Delta E = \Delta V + \Delta E_{\text{line}} - \Delta W$ and the probability of this event in kMC algorithm is obtained from $\Delta G$. If this event is selected, the penetration of the dislocation into the 'f' obstacle is advanced to $y + dy$. Series of tests for different values of $dy$ showed that $dy \leqslant 10^{-4} d_f$ is sufficient for the convergence and accuracy of the overall results. Due to the computational cost, solute obstacles here are still treated as point-pinning obstacles. Once we have the activation barrier $\Delta G_i$ for all barriers $i$ in contact with the dislocation line, we compute the probability of thermal activation across the $i$th barrier as $p_i = \exp(-\frac{\Delta G_i}{k_B T})$s and select a barrier according to the standard Monte Carlo algorithm using a random number $R \in (0, 1)$. In the EO Monte Carlo simulations, each attempted change in the configuration has no associated time. The Monte Carlo process is simply a means of sampling the configuration space to find a path that minimizes the overall activation barrier $\Delta G$ for the process. Therefore, for the EO simulation, we track the total energy of the dislocation during its evolution through the computed thermally activated path and take the highest energy barrier encountered by the dislocation as the overall activation energy.

In the results shown in the next section, all lengths are normalized as $l^* = l/(d_s)$, all forces are normalized as $f^* = f/(\mu b^2)$, and all energies are normalized as $\Delta G^* = \Delta G/\Delta G_s^0$. Simulations at two different temperature $T = 78$ and $312$ K are carried out, corresponding to the normalized thermal energies $k_B T/\Delta G_s^0 = 6.7 \times 10^{-3}$ and $26.8 \times 10^{-3}$ for $\Delta G_s^0 = 1$ eV. All stresses are normalized as $\sigma^* = \sigma d_s/(\mu b)$. Note that $\hat{\sigma}_s^* = 0.9 \cos^{3/2}(\phi_s^c/2)$ [3, 38] and $\hat{\tau}_f^* = \frac{d_s}{d_f} \cos(\phi_f^c/2)$ since the 'f' obstacles are in a periodic linear array. We consider a system with a large density difference between 's' and 'f' obstacles ($d_f \gg d_s$) such that the linear additivity of the zero-temperature flow stress $\hat{\sigma}^* = \hat{\sigma}_s^* + \hat{\sigma}_f^*$ is ensured [19]. In the PP simulation, the time is normalized by $\nu_0$ as $t^* = \nu_0 t$. In the EO simulations, the shear modulus $\mu$ and the magnitude of the Burgers vector $b$ are $\mu = 26$ GPa and $b = 0.286$ nm, corresponding to aluminum alloys. Simulations with different $\phi_f^c$ and $\phi_s^c$ are investigated. The flow stress is the input applied stress $\sigma^*$, and we will also refer to a normalized flow stress $\eta = \sigma^*/\hat{\sigma}^*$.

The results from different simulation models are interpreted in terms of the normalized overall activation energy $\Delta G^*$ as a function of the normalized applied flow stress $\eta$ at temperature $T$. As an example of the direct output of the EO simulation, figure 2 shows the energy variation as the dislocation advances by thermally activated steps when interacting with the extended 'f' obstacle and point-like 's' obstacles, and the highest energy barrier at different $\eta$ is shown. Initially at prescribed applied stress $\eta$, after the dislocation reaches an initial mechanical equilibrium, it then advances further into the extended forest obstacle via small thermal activation processes that are driven by the reduction of the total energy due to the work done by the applied field. Once the dislocation reaches the total energy minimum position, it will then bypass new obstacles and extend further into the extended obstacle with increasing total energy provided by thermal fluctuations. Note that we are interested in the presence of both forest and solute obstacles in the simulation, we have linear additivity at zero $T$ and we focus on the region where the normalized flow stress $\eta \geqslant \hat{\sigma}_s/(\hat{\sigma}_s + \hat{\sigma}_f)$ so that the forests must play a role in restraining the dislocation motion. In all cases, a large number of statistical replicas using the same obstacle parameters but spatial differences of the point-pinning solute obstacles were generated, and the results quoted are the average over all these realizations, with error bars indicating variations among the set of replicas.
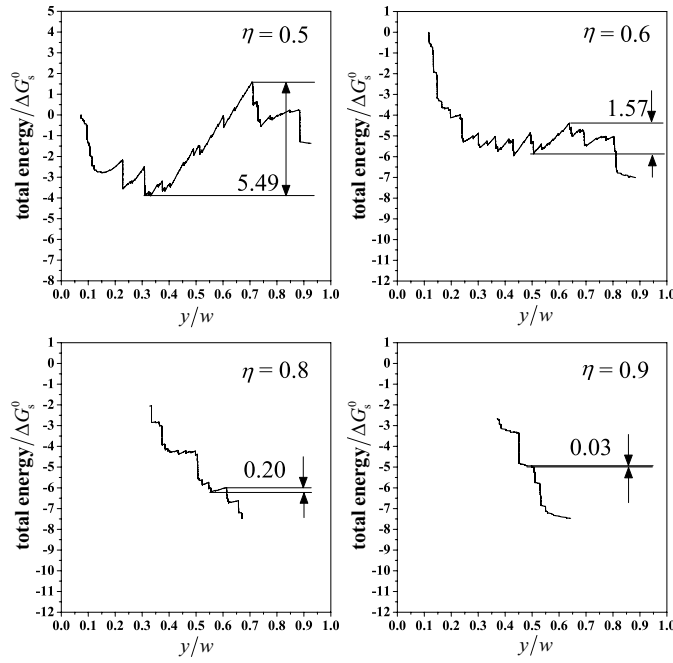
**Figure 2.** Normalized total energy evolution versus dislocation position within the forest obstacle during the thermally activated motion of dislocation glide through the mixed-type obstacles for different applied stresses, with the energy barrier indicated. Obstacle properties $\hat{\sigma}_s^* = 8.5 \times 10^{-4}$, $\hat{\sigma}_f^* = 15 \times 10^{-4}$ and $\Delta G_f^{0*} = 30 (w_f^* = 11.3)$.

## 3. Results and discussion

### 3.1. Single obstacle results

Before starting thermal activation behavior in the system with mixed-type obstacle strengthening, plastic flow in the presence of single obstacle type at finite temperature is investigated to validate the basic models and simulation methods. We have shown that for random point obstacles the activation energy should follow equation (6) while for periodic obstacles the activation energy should satisfy equation (7).

Thermally activated motion of the dislocation in presence of 's' obstacles alone is first simulated via the PP simulation. Figure 3(*a*) shows the analytical model of equation (6) and the numerical results for the activation energy at different flow stress, and excellent agreement is achieved. This confirms that the Friedel limit is still valid at finite temperature for random positioned point-pinning obstacles. Therefore, in following analysis, equation (6) is used to characterize the finite-temperature flow behavior of the solute-strengthening system. The EO simulation is then used to simulate thermal activation over the extended forest obstacles in the absence of solutes. The results are shown in figure 3(*b*) and confirm that equation (7) is quantitatively accurate for a linear array of forest obstacles, validating the EO simulation method implemented. Therefore, we will use equation (7) to characterize the thermal activation of dislocations past the extended forest obstacles.
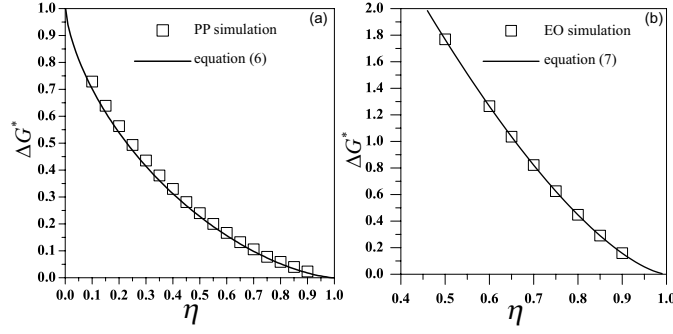
**Figure 3.** Activation energy versus normalized flow stress by a single obstacle type. (*a*) Solute obstacles only, with $\hat{\sigma}_s^* = 8.5 \times 10^{-4}$; (*b*) extended forest obstacles only, with $\hat{\sigma}_f^* = 25 \times 10^{-4}$ and $\Delta G_f^{0*} = 5$.
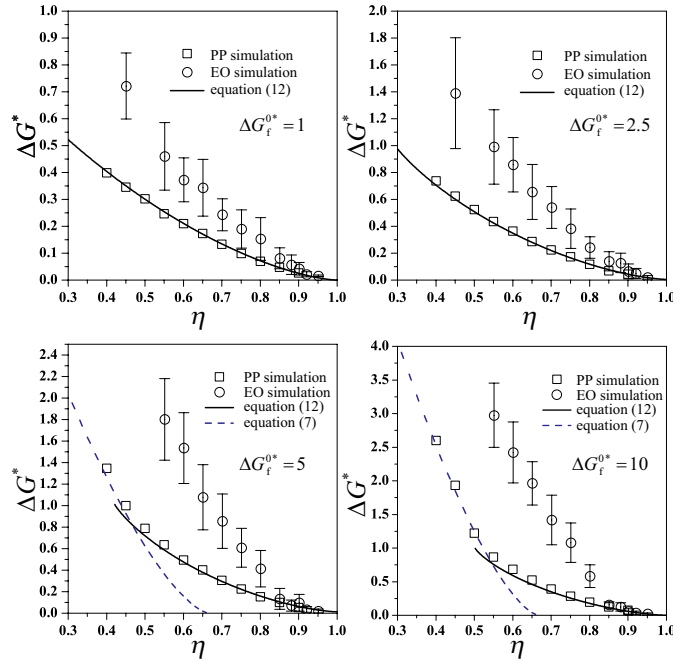


**Figure 4.** Overall activation energy $\Delta G^*$ versus normalized flow stress $\eta$, for different values of the zero-stress activation energy $\Delta G_f^{0*}$, for $\hat{\sigma}_s^* = 8.5 \times 10^{-4}$ and $\hat{\sigma}_f^* = 15 \times 10^{-4}$. Symbols: simulation data; black solid lines: equation (12) (Kocks model); blue dashed lines: equation (7).

## 3.2. Mixture of point obstacles

Based on the tests above, the two numerical models can now be used to simulate the plastic flow in the presence of two different types of obstacles. The overall activation energy for dislocation glide through fields with two types of *point-like* obstacles were computed by the PP simulation for different zero-stress forest activation energies $\Delta G_f^{0*}$ ranging from 1 to 10. Figure 4 shows the total activation energy $\Delta G^*$ as a function of the flow stress $\eta$. The dislocation configuration during the thermal motion is shown in figure 5, and is consistent with the physical process proposed by Kocks *et al* [8]. The dislocation line initially reaches a static equilibrium configuration, pinned by both solute obstacles and forest

9
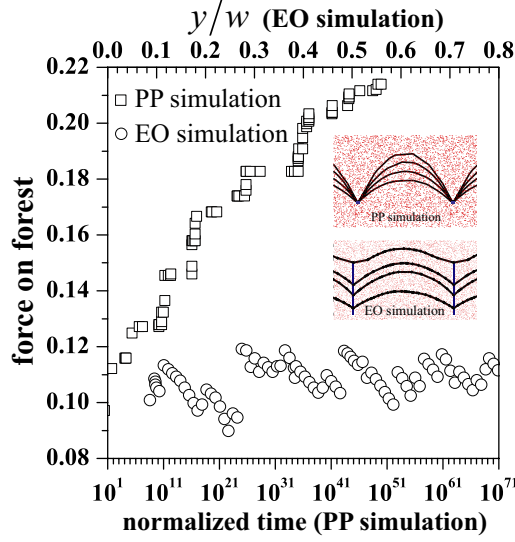
**Figure 5.** Force on the forest obstacles versus the normalized time in the PP simulation and versus the penetration distance of dislocation into the forest in the EO simulation, during the thermal motion of dislocation across the mixed-type obstacle field for one random solute configuration. Inset: evolution of dislocation configuration during thermal activation processes in the PP and EO simulations. Blue bars/dots: forest obstacles; red dots: point solute obstacles; black lines: dislocation. Shown for $\eta = 0.5$, $\Delta G_f^{0*} = 5$, and $\hat{\sigma}_f^* = 15 \times 10^{-4}$.

obstacles. Since the rate for the dislocation to thermally bypass the forest is much lower than that of the solutes, the dislocation continues to bow out by thermal de-pinning from the solutes. The overall curvature of the dislocation line increases, leading to an increase in the force acting on the forest, and hence an increase in the escape rate past the forest. At the critical configuration, the rate of thermal activation over the forest becomes equal or at least comparable to that of the solutes, and thermal activation for dislocation de-pinning from the forest becomes favorable. Once the dislocation escapes from the forest obstacles, the backstress due to the forests is lost and the dislocation moves rapidly through the solute field until it encounters another forest obstacle. Since the activation rate is exponential in the activation energy, the overall time for moving past the forests is dominated by the time spent very near the final configuration just before thermal activation on the forests. The configurational evolution can be quantified by examining the force acting on the forest obstacle during the thermal activation. Figure 5 shows the variation of the force acting on the forest obstacle, $f_f^*$, during the thermal activation in the PP simulations, for one random solute configuration.

Starting with equations (6) and (7) for individual strengthening mechanism, we express the overall activation energy $\Delta G$ as a function of the flow stress $\sigma(\dot{\varepsilon}, T)$ by partitioning $\sigma(\dot{\varepsilon}, T)$ between the two different obstacle resisting the dislocation motion, such that the stress on mechanism 'f' operating in equation (7) is $\sigma_f(\dot{\varepsilon}, T)$ and the stress on mechanism 's' operating in equation is $\sigma(\dot{\varepsilon}, T) - \sigma_f(\dot{\varepsilon}, T)$. Thus we have

$$
\begin{aligned}
\Delta G_s &= \Delta G_s^0 \left( 1 - \left( \frac{\sigma - \sigma_f(\dot{\varepsilon}, T)}{\hat{\sigma}_s} \right)^{2/3} \right)^{3/2} \\
\Delta G_f &= \Delta G_f^0 \left( 1 - \frac{\sigma_f(\dot{\varepsilon}, T)}{\hat{\sigma}_f} \right)^{3/2}.
\end{aligned}
\tag{10}
$$

10

At flow stress, the rate of dislocation escape from both obstacle types are assumed equal [8], and so that the activation energies must be equal to the overall activation energy for the entire process, i.e.

$$\Delta G(\sigma, T) = \Delta G_s(\sigma, T) = \Delta G_f(\sigma, T) \tag{11}$$

$\sigma_f(\dot{\varepsilon}, T)$ can be solved by substituting equation (10) into equation (11). Substituting $\sigma_f(\dot{\varepsilon}, T)$ back into equation (10) and using equation (11) to relate the flow stress $\sigma_f(\dot{\varepsilon}, T)$ with the overall activation energy $\Delta G$ as

$$\sigma = \left(1 - \left(\frac{\Delta G}{\Delta G_s^0}\right)^{2/3}\right)^{3/2} \hat{\sigma}_s \left(1 - \left(\frac{\Delta G}{\Delta G_f^0}\right)^{2/3}\right) \hat{\sigma}_f. \tag{12}$$

Equation (12) is compared with the numerical results obtained from the PP simulation in figure 4, and good agreement is found for a wide rage of obstacle properties.

The model of equation (12), which is hereafter referred to as the Kocks model, must fail when $\Delta G > \Delta G_s^0$, which occurs at low flow stress $\eta$ and large $\Delta G_f^{0*} > 5$. Since the thermal activation rate is exponential in the activation energy, at high $\Delta G_f^{0*} > 5$ the escape rate of the forest obstacles at low stress is so small compared with that of the solutes that the dislocation is pinned only by the forests, and with large activation energy. This is verified by comparing the numerical data in this low-stress regime with the prediction of equation (7), using the total applied stress $\sigma = \eta \left(\hat{\sigma}_s + \hat{\sigma}_f\right)$ acting only on the forests. As shown in figure 4, good prediction is achieved at low $\eta$ and high $\Delta G_f^0$, where the Kocks model fails.

We conclude that if all obstacles are point-like, then (i) at high flow stress and low forest activation energy, the total flow stress at finite temperature $T$ and strain rate $\dot{\varepsilon}$ can be obtained by summing over all individual flow stresses measured at same $T$ and $\dot{\varepsilon}$ and (ii) when $\Delta G_f^0$ is high and the flow stress is low, the thermal activation is controlled by the forests alone, which can also be predicted by a point-based model. Simulations and model predictions for different combinations of $\hat{\sigma}_f$ and $\hat{\sigma}_s$ were also investigated for the point-pinning case, and found to be qualitatively very similar to the case shown in figure 4.

### 3.3. Mixture of extended forests and point solute obstacles

The simulation results for the overall activation energy obtained from the EO simulation are also shown in figure 4, to permit direct comparison between the PP simulation and EO simulation for exactly the same system parameters. The EO and PP simulations only agree at high flow stress, as shown in figure 6 for $\eta > 0.85$ where the Kocks model predictions (matching the PP simulations data not shown) capture the EO simulations well. At such high flow stresses $\eta$, the penetration distance into the extended 'f' obstacle is such that the activation length $y_m - y_e \sim 0.1d_s$ is small compared with the solute spacing. A point-pinning approximation for the forest obstacles is thus reasonable, and linear additivity of the flow stresses follows. Therefore, it is not the total obstacle length $w_f$ that determines whether the forest behaves as a point or extended obstacle, but rather the activation length $y_m - y_e$, which is stress dependent. Generally, $y_m - y_e \sim w_f$ but at sufficiently high stress $y_m - y_e$ can be small enough so that the extended obstacle acts like a point obstacle. At lower flow stresses $\eta < 0.85$, the EO simulations yield values of $\Delta G^*$ that are much larger than obtained from the PP simulations or Kocks model, and the discrepancy increases as $\Delta G_f^{0*}$ increases, i.e. as $w_f$ increases. In this regime, $y_m - y_e > d_s$ and the point obstacle model fails, which is usually coincident with $w_f/d_s > 1$, except at very high stresses.

Figure 7 shows the EO simulation results and the predictions of the Kocks model at $\Delta G_f^{0*} = 5$ for different values of the forest strengthening $\hat{\sigma}_f^*$ with fixed solute
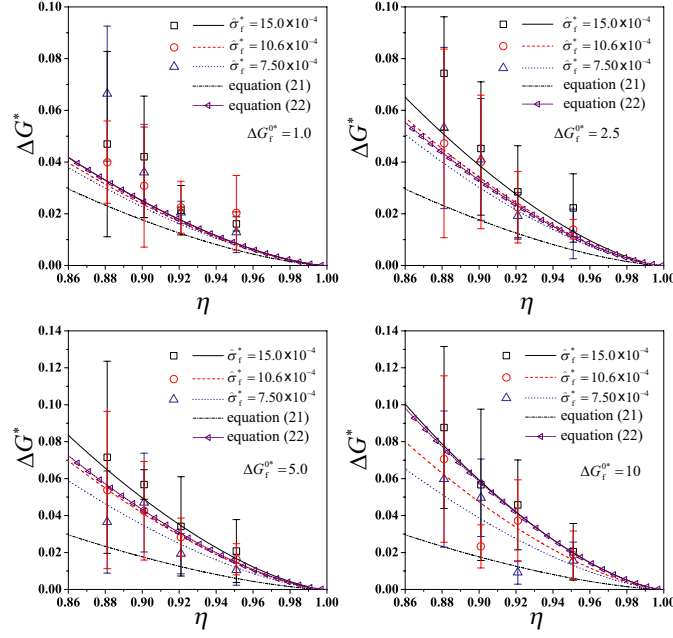
**Figure 6.** Overall activation energy versus normalized flow stress, at high flow stress levels, for $\hat{\sigma}_s^* = 8.5 \times 10^{-4}$ and varying $\hat{\sigma}_f^*$. Symbols: EO simulations; solid/dashed/dotted lines: predictions of the Kocks model, equation (12); dash-dotted lines: predictions of the postulate of Curtin [28]; dot-triangle lines: predictions of the *ad hoc* model, equation (22).
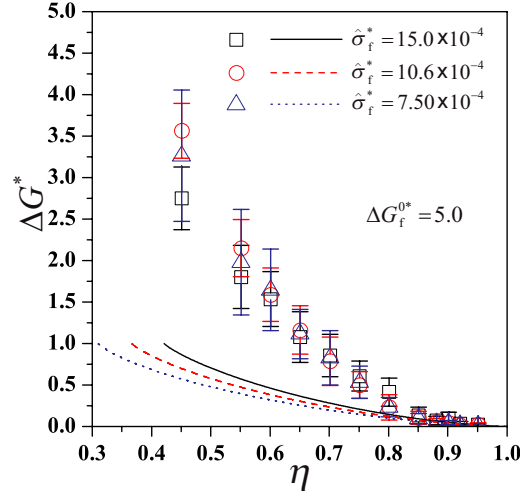


**Figure 7.** Normalized overall activation energy versus applied load, for different forest stresses at fixed solute strength $\hat{\sigma}_s^* = 8.5 \times 10^{-4}$. Symbols: EO simulations; lines: predictions of the Kocks model (equation (12)).

strengthening $\hat{\sigma}_s^*$. Unlike the Kocks model which predicts decreasing activation energy with decreasing forest strength, as shown in figures 6 and 7, the dependence of $\Delta G^*$ on the forest strengthening is negligible, aside its appearance in $\eta$ at a low flow stress level. And since a decreasing forest strength at fixed $\Delta G_f^{0*}$ implies an

increasing $w_f$, the failure of the point-pinning model can again be associated with $w_f/d_s > 1$.

Examination of the dislocation configuration during the thermal activation process in the EO simulation reveals the key difference between PP and EO simulations. The lower inset in figure 5 shows how the dislocation thermally advances in the mixed-type obstacle field for one random solute configuration in the EO simulation. During the activation process, the dislocation gradually moves through the forest obstacle from $y_e$ to the saddle point $y_m$ while maintaining a nearly *constant curvature* during the activation process, corresponding to a *constant force* acting on the forest obstacle. This differs from the PP simulation (upper inset of figure 5), and is very similar to the behavior observed when the forest operates alone.

Based on the EO simulation results, we now develop an analytical model to predict the activation energy for extended forest obstacles operating together with solutes. The observation of a fixed dislocation curvature during thermal activation in the EO simulation suggests that the force acting on the extended forest by the bowing out dislocation line remains constant, on average, during the thermal activation process. From the EO simulations, we can explicitly compute the average force $f_f^*$ acting on the forest obstacle during thermal activation using the simulated dislocation curvature, and then determine the stress acting on the forests as $\sigma_f^* = f_f^*/d_f^*$. Figure 8 shows the measured stress $\sigma_f^*$ acting on the forest versus the flow stress $\sigma^* = \eta(\hat{\sigma}_s^* + \hat{\sigma}_f^*)$ for a fixed $\hat{\sigma}_f^* = 15 \times 10^{-4}$ and various $\hat{\sigma}_s^*$. The calculated values of $\sigma_f^*$ are independent of the zero-stress activation energy $\Delta G_f^{0*}$ and, more importantly, vary linearly with the flow stress $\sigma^*$. This suggests that an effective backstress $\sigma_b^*$ exists due to the solutes acting on the forests, so that $\sigma_f^* = \sigma^* - \sigma_b^*$. The values of $\sigma_b^*$ for different $\hat{\sigma}_s^*$, and for different temperatures, are listed in table 1. We note that the ratio $\sigma_b^*/\hat{\sigma}_s^*$, i.e. the backstress provided by the solutes relative to the zero-temperature solute strength, varies with the temperature $T$, reflecting that the thermal activation through the solute field in between the forests remains operative. Given the stress $\sigma_b^*$ carried by the field of solutes at the flow stress $\sigma(\dot{\varepsilon}, T)$, we can compute the activation energy for the solutes from equation (6) as

$$\Delta G_s = \Delta G_s^0 \left(1 - \left(\frac{\sigma_b}{\hat{\sigma}_s}\right)^{2/3}\right)^{3/2}. \tag{13}$$

Furthermore, with $\sigma_f(\dot{\varepsilon}, T) = \sigma(\dot{\varepsilon}, T) - \sigma_b(T)$, the activation energy for the forest obstacles follows from equation (7) as

$$\Delta G_f = \Delta G_f^0 \left(1 - \frac{\sigma - \sigma_b}{\hat{\sigma}_f}\right)^{3/2}. \tag{14}$$

Combining equation (13) and (14) yields the overall activation energy

$$\Delta G(\sigma, T) = \Delta G_f^0 \left(1 - \frac{\sigma - \sigma_b}{\hat{\sigma}_f}\right)^{3/2} + \Delta G_s^0 \left(1 - \left(\frac{\sigma_b}{\hat{\sigma}_s}\right)^{2/3}\right)^{3/2} \tag{15}$$

where the temperature dependence is implicit through the dependence of $\sigma_b$ on temperature, with the temperature-dependences in $\Delta G^0$ still neglected. Note that equation (15) does not apply when $\sigma > \sigma_b + \hat{\sigma}_f$, where linear additivity (the Kocks model) explains the results, as discussed above. Figure 9 shows the predicted value of $\Delta G^*$ using equation (15) in its range of validity; good agreement is found for all values of $\hat{\sigma}_f^*$ and $\Delta G_f^{0*}$. Similar agreement is found for other solute strength $\hat{\sigma}_s^*$ with the corresponding values of $\sigma_b^*$ listed in table 1. Moreover, the predictions at two different temperatures agree well with the EO simulations, as shown in figure 10.

One key feature of our result is that the activation energy itself depends on temperature in this forest-controlled regime. This is outside the standard modeling of thermally
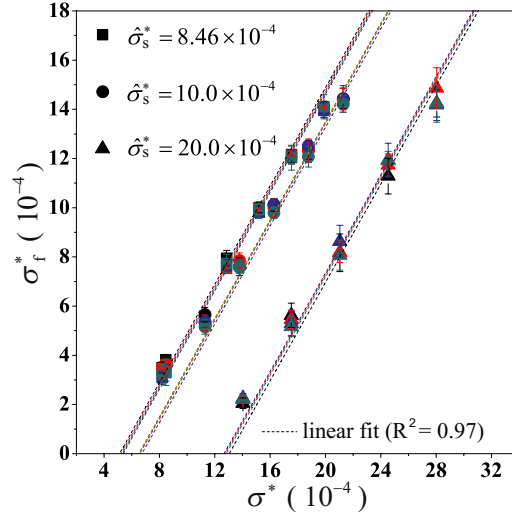
**Figure 8.** Average stress on extended forest obstacle during the thermally activation process versus the applied flow stess, for different forest energy barriers $\Delta G_f^*$ and solute strength $\hat{\sigma}_s^*$ at fixed strength $\hat{\sigma}_f^* = 15 \times 10^{-4}$. Symbol colors in the figure refer to different values of $\Delta G_f^*$; black, $\Delta G_f^{0*} = 1$; red, $\Delta G_f^{0*} = 2.5$; blue, $\Delta G_f^{0*} = 5$; green, $\Delta G_f^{0*} = 10$.

**Table 1.** The fitted values of the effective solute backstress $\sigma_b^*$, for different zero-temperature solute strengths $\hat{\sigma}_s^*$ and different temperatures $T$.

| $T\,(\mathrm{K})$ | $\hat{\sigma}_s^*(\times 10^{-4})$ | $\sigma_b^*(\times 10^{-4})$ | $\sigma_b^*/\hat{\sigma}_s^*$ |
|---|---|---|---|
|    | 8.46 | 5.33 | 0.63 |
| 78 | 10.00 | 6.59 | 0.65 |
|    | 20.00 | 12.60 | 0.53 |
| 312 | 8.46 | 4.02 | 0.48 |

activated processes, but arises because the phenomenon here is controlled by two intersecting thermally activated processes affecting the motion of the dislocation line. The implication of equation (15) is then that the strain rate and temperature are not interchangeable variable through the product $k_B T \ln(\dot{\varepsilon}_0/\dot{\varepsilon})$.

The EO simulations clearly show that the finite interaction length between dislocation and the forest obstacle completely modifies the thermal activation process, compared with the PP simulation, with the stress dependence of the activation barrier (equation (15)) controlled by the forests and with the solutes contributing a fixed increment to the activation barrier. We have no prediction for the measured values of the temperature-dependent effective solute backstress $\sigma_b$, but the analytic model of equation (15) otherwise explains the low-stress regime very well. The high stress regime is adequately explained by the Kocks model (equation (12)). The two models have different values of $\Delta G^*$ right at the 'transition' stress of $\sigma = \sigma_b + \hat{\sigma}_f$ and the slopes are notably different at this point—the transition from the high-stress to low-stress regime is thus not captured by the models here.
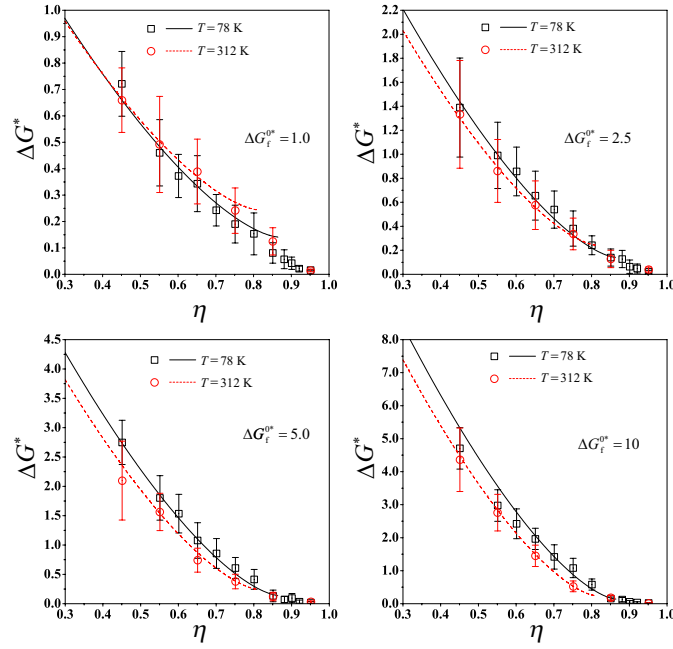
### 3.4. Discussion

The EO simulations confirm the influence of the finite interaction length $w_f$ on the finite-temperature flow stress in the presence of mixed-type obstacles when $w_f \gg d_s$. Equation (15),

14
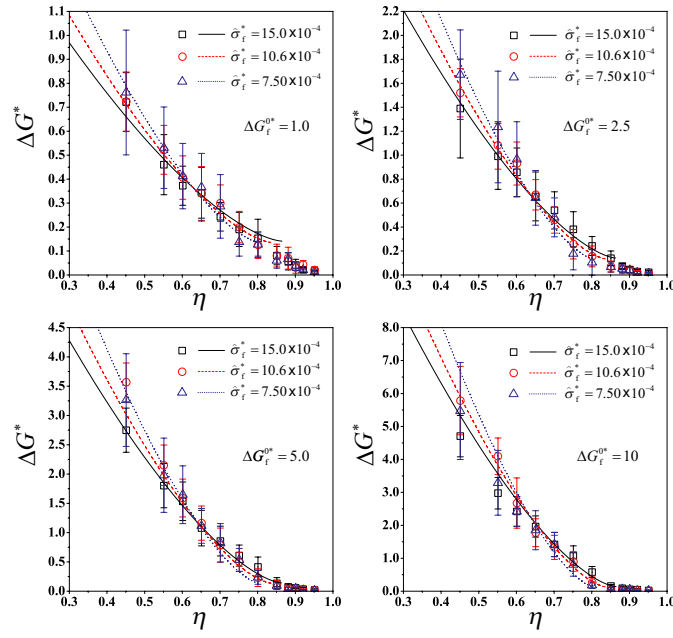
**Figure 9.** Variation of the overall activation energy with flow stress given $\hat{\sigma}_s^* = 8.5 \times 10^{-4}$. Symbols: EO simulations; lines: prediction of equation (15).



**Figure 10.** Variation of the activation energy with flow stress at two different temperature, given $\hat{\sigma}_s^* = 8.5 \times 10^{-4}$ and $\hat{\sigma}_f^* = 15 \times 10^{-4}$. Symbols: EO simulations; lines: prediction of equation (15).

based on EO simulations, accounts for the finite interaction length effect. For pure metals, $\hat{\sigma}_s$ and $\sigma_b$ are both equal to 0 and equation (15) yields equation (7) for the forests operating alone. Overall, our analysis suggests that for extended obstacles at high $\Delta G$, the thermal activation is controlled by the extended forest obstacles while at low $\Delta G$ the thermal activation energy barrier follows the Kocks model. Experimentally, $\Delta G$ is related to the temperature and strain rate at which the experiments are conducted as $\Delta G = k_B T \ln \frac{\dot{\varepsilon}_0}{\dot{\varepsilon}}$, where $\dot{\varepsilon}_0 \sim 10^5 \, \text{s}^{-1}$ is a typical reference strain rate value. In typical experiments, the temperature usually ranges from 78 K to room temperature ($\sim$300 K) and the strain rate from $10^{-5}$ to 0.1 s$^{-1}$, giving the $\Delta G$ values in the range 0.1–0.6 eV. For $\Delta G_s^0 = 1$ eV, as used in our EO simulations and typical of solute-strengthening energetics [7] and $\Delta G_f^0 \sim 5$ eV as derived for Cu [41] our results suggest that experiments over this range of temperatures span $\Delta G^* = 0.1$ to 0.6 and actually cross over between the two regimes described by equations (12) and (15).

To compare with general experimental observations, we now examine the activation area as predicted by the various models. For mixed point obstacles, the linear additivity Kocks model is known to lead to the linear additivity of the inverse activation area [8, 25, 27], so that

$$\frac{1}{\Delta a} = \frac{b}{k_B T} \frac{\partial \left( \sigma_s(\dot{\varepsilon}, T) + \sigma_f(\dot{\varepsilon}, T) \right)}{\partial \ln \dot{\varepsilon}} \bigg|_T = \frac{1}{\Delta a_s} + \frac{1}{\Delta a_f}, \tag{16}$$

where $\Delta a_s$ and $\Delta a_f$ are the activation area at $T$ and $\dot{\varepsilon}$ for solutes and forests, respectively. Since $\sigma_f \sim 1/d_f$ and $\Delta a_f \sim d_f$, we have $1/\Delta a_f = \beta \sigma_f(\dot{\varepsilon}, T)$ leading to the well-known result

$$\frac{1}{\Delta a} = \frac{1}{\Delta a_s} + \beta \left( \sigma(\dot{\varepsilon}, T) - \sigma_s(\dot{\varepsilon}, T) \right) \tag{17}$$

where the slope parameter $\beta$, revealed in a Haasen plot [29], is identical to the slope parameter when the forests operate alone. However, experiments on various solute-strengthened materials at low temperature (corresponding to small $\Delta G = k_B T \ln(\dot{\varepsilon}_0/\dot{\varepsilon})$) show a slightly lower slope than measured in the pure alloy [25, 27].

At high temperatures or very low strain rate, i.e. larger values of $\Delta G = k_B T \ln(\dot{\varepsilon}_0/\dot{\varepsilon})$, we would expect equation (15) to be applicable. From equation (15), the inverse activation area at fixed $\dot{\varepsilon}$ and $T$ is given by

$$\frac{1}{\Delta a} = \frac{3b}{2\Delta G_f^0} \frac{\sigma - \sigma_b}{\left( \frac{k_B T \ln(\dot{\varepsilon}_0/\dot{\varepsilon})}{\Delta G_f^0} - \frac{\Delta G_s}{\Delta G_f^0} \right)^{1/3} - \left( \frac{k_B T \ln(\dot{\varepsilon}_0/\dot{\varepsilon})}{\Delta G_f^0} - \frac{\Delta G_s}{\Delta G_f^0} \right)}, \tag{18}$$

where $\Delta G_s = \Delta G_s^0 \left( 1 - \left( \sigma_b/\hat{\sigma}_s \right)^{2/3} \right)^{3/2}$. In this case, the apparent yield point is $\sigma_b$, and plotting $1/\Delta a$ versus $\sigma - \sigma_b$ yields a zero intercept in the Haasen plot, i.e. no initial activation area $1/\Delta a_s$ at low (near-zero) forest strength. The predicted slope in equation (18) can be either larger or smaller than the slope when forests operate alone, depending on the experimental strain rate and the value of $\Delta G_f^0$. As a consequence, our results here fail to explain the reduced Haasen slope observed in experiments for solute-strengthened alloys at larger $\Delta G$.

With no analytical models matching experiments, we revisit simply the raw simulation data. Given the uncertainty of the simulation results, we could represent the computed activation energy as a function only of the stress variable $\eta$, at any fixed temperature, as

$$\Delta G = \Delta G_s^0 f(\eta, \Delta G_f^0). \tag{19}$$

This form neglects any dependence of $\Delta G$ on $\hat{\sigma}_f$, a dependence that is weakly indicated in our simulations. The activation area based on equation (19) would be

$$\frac{1}{\Delta a} = \frac{1}{\Delta a_0} + \frac{1}{\Delta a_0 \hat{\sigma}_s} \hat{\sigma}_f. \tag{20}$$

16

The slope of the Haasen plot for solute-strengthening alloys would then be consistent with experiments. The intercept value $1/\Delta a_0$ would not, however, necessarily be the value corresponding to the solute-only activation area. But at low temperature and low forest strengthening, where the numerical results are in reasonable agreement with the Kocks model, the intercept value would have to asymptotically approach $1/\Delta a_0 = 1/\Delta a_s$, and this would then agree with the low temperature experiments of Diak *et al*, as shown in [28]. However, the explicit form postulated by Curtin [28]

$$\Delta G = \Delta G_s^0 \left(1 - \eta^{2/3}\right)^{3/2} \tag{21}$$

does not quantitatively agree with the EO simulation results, as shown in figure 6, most notably failing to predict the dependence of the activation barrier on $\Delta G_f^0$. An *ad hoc* form given by

$$\Delta G = \Delta G_s^0 \left(1 + \Delta G_s^0 / \Delta G_f^0\right)^{1/2} \left(1 - \eta^{2/3}\right)^{3/2} \tag{22}$$

yields reasonable results across the entire spectrum of data at high stresses, as shown in figure 6. This form has no formal justification and $1/\Delta a_0 \neq 1/\Delta a_s$, but is of the form of equation (20) that agrees with experiments.

At elevated temperatures and low stresses, the intercept value could differ from the value of the solutes only, reflecting the influence of the forest hardening and forest activation energy. The role of temperature and of the apparent solute backstress that emerges from the simulations would complicate microscopic interpretation of the parameters obtained from the Haasen plot.

Finally, we note that we are unable to computationally probe the limit of $\hat{\sigma}_f \to 0$, i.e. when the initial forest density $\rho_f$ is very low, which corresponds to the very early stages of deformation in a well-annealed alloy. Conclusions drawn about behavior occurring at low levels of forest strengthening must thus be done with caution. The simulations (figure 8) suggest that the backstress $\sigma_b$ is effectively a lower bound on the strength at finite temperature; when $\sigma < \sigma_b$, the forest would contribute an activation energy $\Delta G_f^0$ which is far larger than can be achieved through thermal activation. Resolution of this issue is achieved in part by considering the contributions to the strain rate from dislocation motion through the solutes in regions between the low density of forests, along with the lines of Schoeck [32], leading to an overall strain rate

$$\dot{\varepsilon} = \rho_m b \nu_0 \frac{1}{\sqrt{\rho_f} \exp\left(\frac{\Delta G}{k_B T}\right) + \sqrt{\rho_s} \exp\left(\frac{\Delta G_s}{k_B T}\right)} \tag{23}$$

where $\rho_m$ is the mobile dislocation density, $\Delta G$ is the overall activation energy computed from equation (15), $\rho_s$ is the solute density and $\Delta G_s$ is the activation barrier associated with solute-only field. However, when $\Delta G$ is large, even at very small $\rho_f$ and low $\hat{\sigma}_f$, the thermal activation energy is dominated by the forest. This conclusion is similar to Picu's [34] observation that the SRS parameter is very sensitive to the existence of 'strong' obstacles.

In all simulations presented here and in previous investigations, the solute obstacles are always treated as point-like obstacles, i.e. the interaction length $w_s$ is assumed small and thus ignored. Since the EO simulation has clearly shown that it is important to consider the extent of the obstacle at finite temperature, the point assumption for the solutes may also not be valid. In fact, solute strengthening at moderate concentrations is controlled by collections of solutes in favorable and unfavorable statistically occurring configurations. It thus remains necessary to improve our understanding of how to model true solute strengthening with forest hardening. Treating both mechanisms as finite-size obstacles is one direction, but this requires large, possibly unachievable, computational cost. We are pursuing an alternative path of examining dislocation interactions in a solute-strengthening environment at the atomistic scale via molecular dynamics, but only at $T = 0$, and will report on this work in future.

17

## 4. Summary

In summary, we have numerically and theoretically studied the plastic flow in the presence of two different obstacle strengthening mechanisms, especially focusing on the influence of a finite dislocation–obstacle interaction length on the rate- and temperature-dependent flow stress. Our results show that the linear additivity of the flow stress due to different strengthening mechanisms can be extended from zero temperature to finite temperature only when all strengthening obstacles are point-like obstacles. Finite-length interactions between dislocation and forest obstacles become important when $w_f \gg d_s$, i.e. when the forest interaction length is longer than the spacing between the point obstacles. In this regime, the solutes appear to exert a constant backstress on the forest dislocation during the thermal activation process, and we have proposed an analytical model reflecting this behavior and agreeing well with our simulations with no adjustable parameters. We have discussed the implications of our simulations on interpretations of experimental data, in particular the activation area. Discrepancies remain between all analytical models and experiments, although a generic and *ad hoc* fitting of our data could show the general trend exhibited by experiments (equation (22)). While our simulations are perhaps the most extensive ever undertaken for this problem, the limitations of a line-tension model, point solute obstacles and simple extended forest obstacles, may not lead to sufficiently accurate physical insights to aid in understanding detailed thermally activated deformation in metal alloys. This points toward more-detailed simulation methods and multiscale models as a means to capture true atomistic response of the dislocation/solute/forest junction interactions.

## Acknowledgments

## References

[1] Mott N F 1956 *Atomic Structure and the Strength of Metals* (New York: Pergamon)
[2] Fleischer R L 1963 Substitutional solution hardening *Acta Metall.* **11** 203–9
[3] Friedel J 1964 *Dislocations* (Oxford: Pergamon)
[4] Trinkle D R and Woodward C 2005 The chemistry of deformation: how solutes soften pure metals *Science* **310** 1665–7
[5] Argon A S 2008 *Strengthening Mechanisms in Crystal Plasticity* (Oxford: Oxford University Press)
[6] Bacon D J, Osetsky Y N and Rodney D 2009 Dislocation-obstacle interactions at the atomistic level *Dislocations in Solids* **15** 1–90
[7] Leyson G P M, Curtin W A, Hector L G and Woodward C F 2010 Quantitative prediction of solute strengthening in aluminium alloys *Nature Mater.* **9** 750–5
[8] Kocks U F, Argon A S and Ashby M F 1975 Thermodynamics and kinetics of slip *Prog. Mater. Sci.* **19** 1–281
[9] Caillard D and Martin J L 2003 *Thermally Activated Mechanisms in Crystal Plasticity* (Boston, MA: Pergamon)
[10] Koppenaal T J and Kuhlmann-Wilsdorf D 1964 The effect of prestressing on the strength of neutron-irradiated copper single crystals *Appl. Phys. Lett.* **4** 59–61
[11] Hiratani M and Bulatov V V 2004 Solid-solution hardening by point-like obstacles of different kinds *Phil. Mag. Lett.* **84** 461–70
[12] Foreman A J E and Makin M J 1967 Dislocation movement through random arrays of obstacles *Can. J. Phys.* **45** 511–7
[13] Hanson K and Morris J J W 1975 Estimation of the critical resolved shear stress for dislocation glide through a random mixture of distinct obstacles *J. Appl. Phys.* **46** 2378–83

[14] Hanson K, Altintas S and Morris J W Jr 1976 Computer simulation of dislocation glide through fields of point obstacles *Conf. on Computer Simulation for Materials Applications (Gaithersburg, MD)* pp 917–28

[15] Zhu A W, Csontos A and Starke E A 1999 Computer experiment on superposition of strengthening effects of different particles *Acta Mater.* **47** 1713–21

[16] Ebeling R and Ashby M F 1966 Dispersion hardening of copper single crystals *Phil. Mag.* **13** 805–34

[17] Reppich B, Kuhlein W and Meyer G 1986 Duplex gamma particle hardening of the superalloy nimonic PE 16 *Mater. Sci. Eng.* **83** 45–63

[18] Lagerpusch U, Mohles V, Baither D, Anczykowski B and Nembach E 2000 Double strengthening of copper by dissolved gold-atoms and by incoherent $SiO_2$-particles: how do the two strengthening contributions superimpose? *Acta Mater.* **48** 3647–56

[19] Dong Y, Nogaret T and Curtin W A 2010 Scaling of dislocation strengthening by multiple obstacle types *Metall. Mater. Trans.* A **41** 1954–60

[20] Monnet G and Devincre B 2006 Solute friction and forest interaction *Phil. Mag.* **86** 1555–65

[21] Altintas S, Hanson K and Morris J W 1976 Computer-simulation of plastic-deformation through planar glide in an idealized crystal *J. Eng. Mater. Technol.—Trans. ASME* **98** 86–91

[22] Arsenault R J and Li S 1989 Computer-simulation of thermally activated dislocation-motion: III. In fcc solid-solutions *Metal. Trans.* A **20** 1429–37

[23] Xu Z J and Picu R C 2007 Thermally activated motion of dislocations in fields of obstacles: The effect of obstacle distribution *Phys. Rev.* B **76** 094112

[24] Kocks U F 1985 Kinetics of solution hardening *Metall. Trans.* A **16** 2109–29

[25] Diak B J, Upadhyaya K R and Saimoto S 1998 Characterization of thermodynamic response by materials testing *Prog. Mater. Sci.* **43** 223–363

[26] Mulford R A 1979 Analysis of strengthening mechanisms in alloys by means of thermal-activation theory *Acta Metall.* **27** 1115–24

[27] Diak B J and Saimoto S 1997 The determination of solute clusters in dilute aluminum alloys using strain rate sensitivity *Mater. Sci. Eng.* A **234–236** 1019–22

[28] Curtin W A 2010 New interpretation of the Haasen plot for solute-strengthened alloys *Scr. Mater.* **63** 917–20

[29] Haasen P 1958 Plastic deformation of nickel single crystals at low temperatures *Phil. Mag.* **3** 384–418

[30] Kocks U F 1979 Superposition of alloy hardening, strain hardening and dynamics recovery *Proc. 5th Int. Conf. on the Strength of Metals and Alloys (Aachen, Germany, 27–31 August 1979)* vol 3 ed P Haasen, V Gerold and G Kosterz (Oxford: Pergamon) pp 166–80

[31] Follansbee P S, Gray G T 1989 An analysis of the low-temperature, low and high strain-rate deformation of Ti–6Al–4V *Metall. Trans. A-Phys. Metall. Mater. Sci.* **20** 863–74

[32] Schoeck G 1985 The superposition of thermal-activation in dislocation movement *Phys. Status Solidi* a **87** 571–81

[33] Arsenault R J and Cadman T W 1974 Kinetics of a dislocation surmounting two different strength barriers *Phys. Status Solidi* a **24** 299–304

[34] Picu R C, Li R and Xu Z 2009 Strain rate sensitivity of thermally activated dislocation motion across fields of obstacles of different kind *Mater. Sci. Eng.* a **502** 164–71

[35] Picu R C and Li R 2010 On the superposition of flow stress contributions at finite temperatures and in the athermal limit *Acta Mater.* **58** 5443–6

[36] Schwarz R B and Labusch R 1978 Dynamic simulation of solution hardening *J. Appl. Phys.* **49** 5174–87

[37] Zhu A and Starke E A 1999 Strengthening effect of unshearable particles of finite size: a computer experimental study *Acta Mater.* **47** 3263–9

[38] Nogaret T and Rodney D 2006 Finite-size effects in dislocation glide through random arrays of obstacles: line tension simulations *Phys. Rev.* B **74** 134110

[39] Olmsted D L, Hector J L G and Curtin W A 2006 Molecular dynamics study of solute strengthening in Al/Mg alloys *J. Mech. Phys. Solids* **54** 1763–88

[40] Leyson G P M, Curtin W A, Hector L G and Woodward C F 2012 unpublished

[41] Follansbee P S and Kocks U F 1988 A constitutive description of the deformation of copper based on the use of the mechanical threshold stress as an internal state variable *Acta Metall.* **36** 81–93

[42] Dupuy L and Fivel M C 2002 A study of dislocation junctions in FCC metals by an orientation dependent line tension model *Acta Mater.* **50** 4873–85

[43] Rodney D and Phillips R 1999 Structure and strength of dislocation junctions: an atomic level analysis *Phys. Rev. Lett.* **82** 1704–07